Chapter 20

Cloud System Modeling

Steven K. Krueger
Department of Meteorology, University of Utah, Salt Lake City, Utah

I. INTRODUCTION

A. WHAT IS A CLOUD RESOLVING MODEL?

A cloud resolving model (CRM) is a 2-D or 3-D model that resolves cloud-scale motions while simulating a cloud system. The scales of motion that are explicitly represented thus depend on the cloud system of interest (Fig. 1). For example, to simulate a convective cloud system that contains both cumulus-scale and mesoscale circulations, a CRM would typically have a horizontal grid size of about 2 km, and a horizontal domain size of about 400 km.

It is interesting to compare the time scales and space scales of a CRM used to simulate a convective cloud system to those of global climate models (GCMs) (Table I). The scales are set by the characteristics of the dominant resolved eddies: cumulus clouds in CRMs, and baroclinic eddies in GCMs. The scales of cumulus clouds are about a hundredth of those of
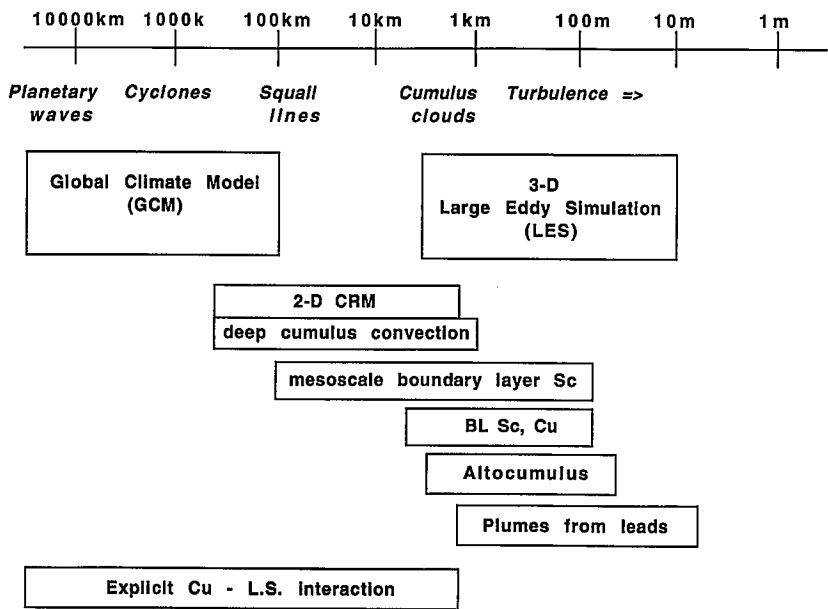
605

| 10000km | 1000k | 100km | 10km | 1km | 100m | 10m | 1m |

Planetary   Cyclones   Squall   Cumulus   Turbulence =>
waves   lines   clouds

```
┌─────────────────────────┐                ┌──────────────────────────┐
│  Global Climate Model   │                │           3-D            │
│         (GCM)           │                │  Large Eddy Simulation   │
│                         │                │          (LES)           │
└─────────────────────────┘                └──────────────────────────┘

        ┌──────────────────────────┐
        │         2-D CRM          │
        ├──────────────────────────┤
        │ deep cumulus convection  │
        └──────────────────────────┘
            ┌──────────────────────────────┐
            │ mesoscale boundary layer Sc  │
            └──────────────────────────────┘
                    ┌──────────────────┐
                    │    BL Sc, Cu      │
                    └──────────────────┘
                    ┌──────────────────┐
                    │   Altocumulus    │
                    └──────────────────┘
                        ┌────────────────────┐
                        │ Plumes from leads  │
                        └────────────────────┘
    ┌──────────────────────────────────┐
    │  Explicit Cu - L.S. interaction  │
    └──────────────────────────────────┘
```

Figure 1 The scales of motion that are explicitly represented by various numerical models of the atmosphere.

Table I
CRMs and GCMs: A Scale Comparison

Aspect	CRM	GCM
Eddies	Cumulus clouds	Baroclinic eddies
Eddy time scale	3×10^3 sec	3×10^5 sec
Forcing time scale	3–4 days	365 days
Domain size	400 km	40,000 km
Horizontal grid size	2 km	200 km
Time step	10 sec	10^3 sec

baroclinic eddies. Thus, a 30-day CRM simulation is equivalent to a 10-year GCM simulation. CRMs have appropriately been called "cloud GCMs."

Both Fig. 1 and Table I make evident that cumulus clouds are not resolved by GCMs: they are sub-grid-scale. Therefore, their collective effects must be parameterized in a GCM. This is difficult. Because CRMs resolve cumulus clouds, a CRM can simulate an ensemble of cumulus

clouds, and the results can be used to test or develop various aspects of cumulus parameterizations.

Although CRMs were originally developed for studying convective cloud systems (e.g., Soong and Ogura, 1980; Soong and Tao, 1980), 2-D versions have recently been applied to shallow convecting layers, such as the atmospheric boundary layer. In this case, the horizontal grid size is about 50 m, and the horizontal domain size about 5 km, and a more appropriate name is eddy-resolving model (ERM) because the large convective eddies are explicitly represented, even though the model is 2-D. Because ERMs are 2-D, they are intermediate in terms of physical realism (and computational cost) between the 1-D models used in GCMs to represent shallow convective layers and 3-D large-eddy simulation (LES) models.

In CRMs, the effects of scales of motion that are not resolved are parameterized using a turbulence closure, whereas the effects of scales larger than the domain size (the "large-scale forcing") must be specified. In addition, turbulent surface transfer, cloud microphysical, and radiative transfer processes are parameterized.

Given the large-scale forcing and the surface properties, a CRM is able to determine the evolution of a cloud system directly, to the extent that its representation of grid-scale dynamics and the parameterizations of its own sub-grid scale processes are accurate.

B. The University of Utah Cloud Resolving Model

Under the direction of Akio Arakawa, a 2-D (x-z) CRM was constructed at UCLA by Krueger (1985, 1988) to simulate cumulus ensembles. The model is based on the anelastic set of equations. It includes a third-moment ensemble-mean turbulence closure. Turbulent surface fluxes are diagnosed using flux-profile relationships based on Monin−Obukhov surface layer similarity theory (Businger *et al.*, 1971). Many improvements to the physics have been incorporated since 1985. The current University of Utah version includes the Coriolis force and the y component of the velocity and a diagnostic turbulent length scale (Xu and Krueger, 1991), a turbulent-scale condensation scheme (Chen 1991), a bulk ice-phase microphysics parameterization (Lord *et al.*, 1984; Krueger *et al.*, 1995a; Fu *et al.*, 1995), and an advanced solar and infrared radiation code (Fu, 1991; Fu *et al.*, 1995; Krueger *et al.*, 1995b).

The surface properties, including the surface temperature and ground wetness, can be specified as functions of time and horizontal position. The lateral boundary conditions are cyclic. The time-varying profiles of the large-scale horizontal advective tendencies of potential temperature and

water vapor are prescribed. The time-varying profiles of the large-scale vertical advective tendencies of potential temperature and water vapor may also be prescribed, or they may be calculated using a specified large-scale vertical velocity profile and the predicted vertical gradients of potential temperature and water vapor. Large-scale forcing for the horizontal velocity may consist of specifying the time-varying profile of geostrophic velocity, or may be included as a nudging toward a specified time-varying profile.

C. What Is a CRM Good For?

CRMs have been extensively used for simulating convective cloud systems. How good are they for this purpose? Similar to GCMs, spatial resolution and sub-grid-scale physics are issues. Unlike GCMs, dimensionality and lateral boundary conditions (i.e., large-scale forcing) are additional issues. Recently, concerted efforts have been made to evaluate CRM simulations of convective cloud systems observed during GATE and TOGACOARE (e.g., Grabowski et al., 1996; Xu and Randall, 1996; Wu et al., 1998; Redelsperger et al., 2000; Krueger et al., 2000).

What is the appropriate horizontal grid size for simulating convective cloud systems? The philosophy is the same as for GCMs and LES models: Resolve the large eddies that do most of the transport. In deep convective cloud systems, these eddies are the tall convective towers (the "hot towers" of Riehl and Malkus, 1958). A horizontal grid size of 1–2 km is generally adequate to resolve these clouds.

Within the boundary layer (often called the subcloud layer), as well as within clouds, smaller turbulent eddies play a significant role. Turbulent eddies do most of the vertical transport in the boundary layer except in the vicinity of convective cloud systems, where cumulus-scale and mesoscale circulations are also important. Aircraft observations made during TOGA-COARE in the vicinity of active cumulus convection indicate that boundary layer motions at spatial scales of less than 2 km exhibit the characteristics of 3-D turbulence, whereas motions on larger scales have quite different characteristics (Williams et al., 1996). This further justifies the use of a horizontal grid size of 1–2 km when using (2-D or 3-D) CRMs to simulate active cumulus convection. Thus, in a CRM, the turbulence closure parameterizes the vertical transport due to boundary layer turbulence as well as the horizontal transport into clouds (i.e., entrainment) due to in-cloud turbulence.

Is it appropriate to use 2-D CRMs to simulate convective cloud systems? The philosophy has been that 3-D CRMs need to be used if the 3-D

structure of the cloud system is the object of the study (e.g., supercells). However, if the goal is to study the statistical (i.e., area-averaged) characteristics of a cloud system, especially in relation to the imposed large-scale forcing, then 2-D simulations appear to be adequate. They typically produce results that are statistically nearly identical to those from 3-D simulations except for larger temporal variability (e.g., Grabowski *et al.*, 1998).

Are the microphysical parameterizations now used in CRMs adequate to simulate convective cloud systems? McCumber *et al.* (1991) concluded that a three-ice-category (cloud ice, snow, graupel/aggregates) bulk parameterization allows a CRM to produce the characteristic radar reflectivity features of tropical squall lines. More recent studies (Redelsperger *et al.*, 2000) indicate that including the ice phase is needed to reproduce the observed dynamical structure of a tropical squall line.

Krueger *et al.* (1995a) found that the microphysics scheme used by Lord *et al.* (1984) underpredicted cloud ice amounts, and hence the horizontal extent of anvil clouds, in simulated tropical squall lines. These upper tropospheric stratiform clouds have a significant radiative impact on the global energy budget. Krueger *et al.* (1995a) modified the microphysics scheme so that it produces more cloud ice. Fu *et al.* (1995) compared the results of the modified scheme to the observations of cloud ice presented by Heymsfield and Donner (1990) and found good agreement.

In a recent CRM intercomparison of multiday simulations of convection during TOGACOARE, differences in microphysical and radiative transfer parameterizations produced significant differences in the cloud radiative forcings (Krueger *et al.*, 2000). Due to the uncertainties in many aspects of the microphysical parameterizations used by CRMs, it may be necessary in the short term to tune the parameterizations so that the top-of-atmosphere radiative fluxes predicted by the CRMs match those observed, similar to how GCMs have tuned their cloud schemes. Unfortunately, this tuning is not as simple or straightforward as it is for GCMs because CRM simulations of GATE and TOGACOARE cloud systems may be significantly affected by inaccuracies in the specification of the large-scale forcing, particularly by the lack of observations of large-scale horizontal advective tendencies of condensate.

As mentioned previously, CRMs have recently been used much like LES models to simulate shallow convective layers. Table II compares the features of 2-D CRMs that explicitly represent the large convective boundary layer eddies (called eddy-resolving models or ERMs) with those of 1-D turbulence closure models (TCMs) and 3-D LES models. Obviously, a 2-D model cannot explicitly represent the 3-D structure of the large turbulent eddies. However, intercomparisons of simulations of a stratocumulus-

Table II
Comparison of Convective Boundary Layer Models

	1-D Turbulence closure	2D CRM/ERM	3D LES
Explicitly represented circulations	None	Mesoscale and large convective eddies	Large turbulent eddies
Parameterized circulations	Clouds and turbulence	3-D turbulence	Small turbulent eddies
Cloud-regime-specific input required	Turbulent length scale Condensation scheme	None	None
Vertical domain	3 km	3 km	3 km
Horizontal domain	(none)	5 km	5×5 km
Grid size	50 m	50×50 m	$50 \times 50 \times 50$ m

topped convective boundary layer with four 2-D CRMs and eight 3-D LES codes by Moeng *et al.* (1996) indicate that the evolution, mean profiles, and scalar flux profiles produced by the two types of models are quite similar, although the turbulent kinetic energy, vertical velocity variance, horizontal velocity variance, and convective mass flux profiles are significantly different due to the differences in the resolved-eddy structure. In the 2-D CRMs, the resolved eddies are roll-like, whereas in the 3-D LES codes, they are plume-like. In addition, the x-component momentum flux profiles are much different due to the differences in large-eddy structure.

Two-dimensional CRMs used as ERMs are more general than 1-D TCMs for simulating shallow convective layers because the large eddies are explicitly represented. As a result, the ERMs do not require the cloud-regime-specific input (turbulent length scale and fractional cloudiness scheme) that the TCMs require (Krueger and Bergeron, 1994). This aspect of ERMs, combined with their computational economy compared to LES codes, makes ERMs an attractive intermediate level model. Their most notable use to date has been for simulating the Lagrangian evolution of the subtropical marine boundary layer (see Section IV).

D. CLOUD PROCESS STUDIES WITH THE UCLA / UU CRM

Most of the studies done with the UCLA/UU (University of Utah) CRM have focused on deep convection over the Tropical oceans. Recently, several studies of shallow convective layers have also been performed. In this chapter, I describe several studies in which I have participated. These

were selected to illustrate how a CRM can be used to better understand cloud processes. Two studies involve deep tropical convection. Section II discusses interactions between radiation and convection in tropical cloud clusters, and Section V deals with the enhancement of surface fluxes by tropical convection. The two intervening sections describe studies of shallow convective layers. Section III describes thin midlevel stratiform (altocumulus) clouds, and Section IV describes the stratocumulus-to-trade cumulus transition in the subtropical marine boundary layer. Section VI presents some results from a study of plumes generated by Arctic leads.

II. INTERACTIONS BETWEEN RADIATION AND CONVECTION IN TROPICAL CLOUD CLUSTERS

The results of this study were published in 1995 by Fu *et al.* (hereafter, FKL95). The goal was to better understand the interactions of infrared (IR) radiation and convection in tropical squall cloud clusters on the time scales and space scales of an individual cloud system (about 500 km and 12 hr). The life cycle of a tropical squall line was simulated over a 12-hr period using thermodynamic and kinematic initial conditions as well as large-scale advective forcing typical of a GATE Phase III squall cluster environment.

To study the impact of IR radiation, we performed three simulations: R1, with no radiative cooling; R2, with only clear-sky radiative cooling; and R3, with fully interactive radiative cooling. The differences between R2 and R1 thus represent the effects of *clear-sky IR radiative forcing*, whereas the differences between R3 and R2 reveal the effects of *IR cloud radiative forcing*. The radiative heating rate profiles for the three simulations are shown in Fig. 2.

The differences between the three simulations are primarily due to the differences in radiative forcing because of the highly organized nature of the simulated convective system. To ensure that such a system developed, the initial wind profile that we used was obtained from a multiday simulation described in Xu *et al.* (1992) during a period in which a long-lived squall line developed. In addition, we introduced a cold pool to initiate the squall line.

To illustrate the life cycle and structure of a typical simulated convective cloud system, Fig. 3 shows snapshots of the total hydrometeor mixing ratio, including cloud water, cloud ice, rain, snow, and graupel, based on the R3 simulation at three different times. In the incipient stage (Fig. 3a), the cloud system consists of isolated precipitating convective towers. In the
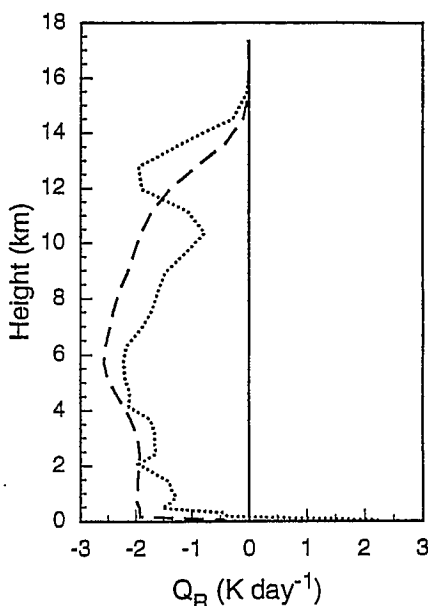
Figure 2 The time- and domain-averaged radiative heating rate profiles for the three simulations (R1, solid; R2, dashed; R3, dotted). [From Fu *et al.* (1995). Reprinted with permission from the American Meteorological Society.]

mature stage (Fig. 3b), new cumulonimbus cells grow at the leading edge of the mesoscale convective system, while older cells successively join the anvil cloud, which has a horizontal extent of about 180 km. At this time, significant precipitation covers a region about 140 km wide. In the dissipating stage (Fig. 3c), little precipitation remains, and the upper-tropospheric stratiform clouds are thinning.

Figure 4 illustrates the effects of clear-sky and cloud IR radiative forcing on the surface precipitation rate during simulations R1, R2, and R3. A comparison of R2 and R1 shows that the clear-sky IR radiative forcing increases the surface precipitation rate throughout the simulation. A comparison of R3 and R2 shows that the cloud IR radiative forcing has essentially no impact until the time of the peak surface precipitation rate (at 280 min), and acts to decrease the surface precipitation rate thereafter. Figure 5c in FKL95 (a time-height cross section of domain-averaged cloud radiative forcing) shows that the cloud radiative forcing does not become significant until about this time. Figure 4 in FKL95 (Hovmöller diagrams of cloud-top temperature for each simulation) shows that significant cloud radiative forcing does not occur until the anvil cloud becomes extensive.
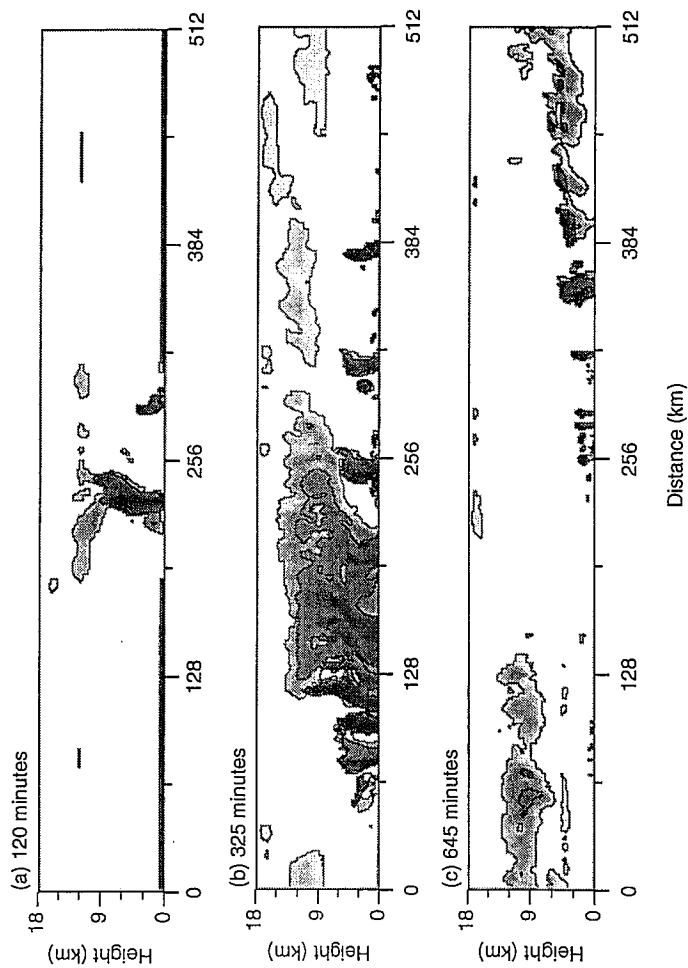
Figure 3 Snapshots (x-z sections) of the total hydrometeor mixing ratio, including cloud water, cloud ice, rain, snow, and graupel, based on the R3 simulation at (a) 120, (b) 325, and (c) 645 min. The shading is proportional to the logarithm of the mixing ratio: Black indicates mixing ratios greater than 10^{-2} and white those less than 10^{-6}. The contours represent mixing ratios of 10^{-4} and 10^{-6}.
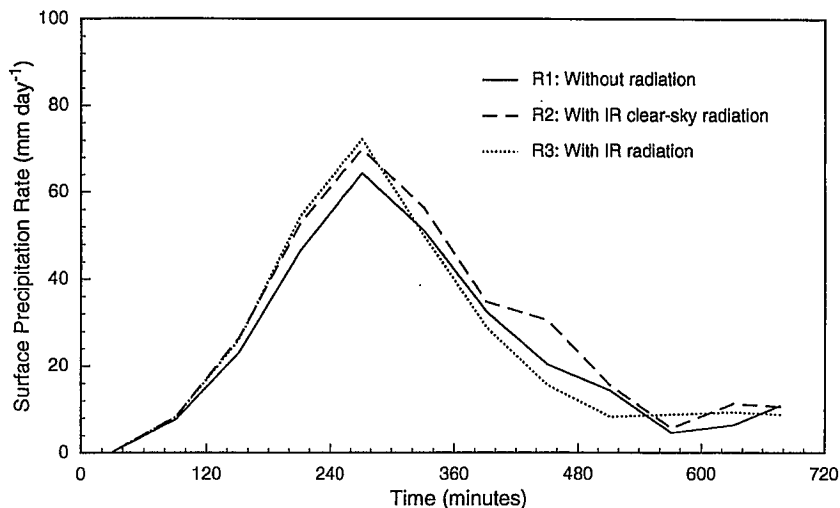
Figure 4   Time series of the surface precipitation rate for the three simulations.

The greater extent of the anvil clouds decreases the outgoing IR flux at the top of the atmosphere by as much as 20 W m^{-2}. This figure also shows that the anvil cloud becomes more extensive in R3 than in R2.

With fully interactive IR radiative heating, direct destabilization of the anvil clouds via IR cloud-top radiative cooling and cloud-base radiative warming (relative to the clear-sky IR cooling rate; see Fig. 2) generates more in-cloud turbulence and contributes to the longevity and extent of the anvil clouds. Figure 5 shows that the time- and domain-averaged cloud fraction at 12 km increases about 0.1 due to cloud radiative forcing, and that this is associated with a marked enhancement of the turbulent kinetic energy within the anvil cloud.

Figure 6 is a schematic illustration of the interactions of IR radiation and convection examined in FKL95's study. It shows that IR clear-sky radiation tends to destabilize the troposphere by cooling it, while IR cloud radiative forcing (due to the radiative effects of the anvil cloud) tends to stabilize the troposphere below 10 km by warming it (relative to IR clear-sky cooling). IR cloud radiative forcing also tends to destabilize the anvil cloud layer from 10 to 14 km, which thereby increases the extent and longevity of the anvil clouds, and thus feeds back to the IR cloud radiative forcing.
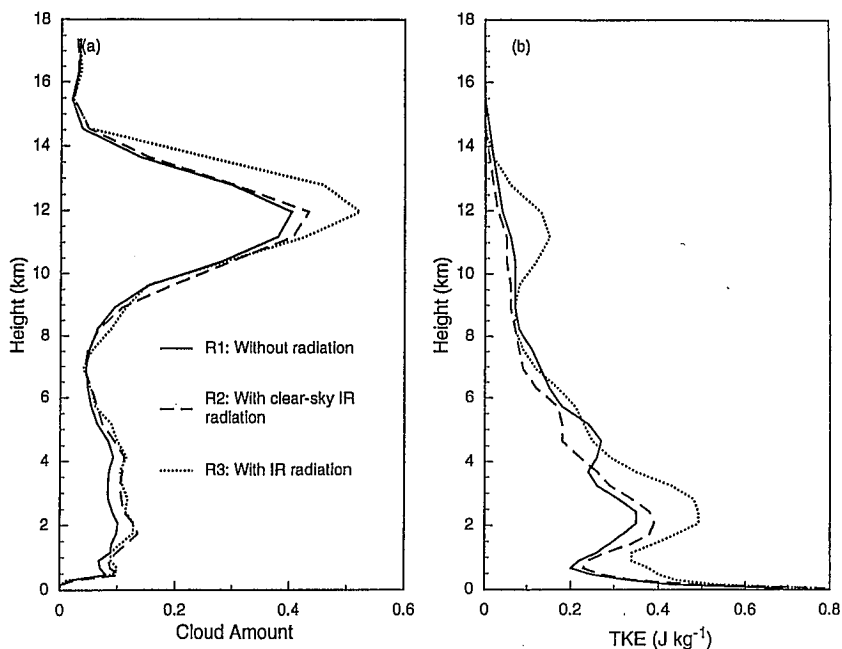
Figure 5 The time- and domain-averaged (a) cloud fraction and (b) turbulent kinetic energy (TKE) profiles for the three simulations. [From Fu *et al.* (1995). Reprinted with permission from the American Meteorological Society.]

III. THIN MIDLEVEL STRATIFORM (ALTOCUMULUS) CLOUDS

Altocumulus (Ac) and altostratus (As) clouds together cover approximately 22% of the Earth's surface (Warren *et al.*, 1986, 1988). Thus, they may play an important role in the Earth's energy budget through their effects on solar and infrared (IR) radiation. However, Ac clouds have been little investigated by either modelers or observational programs.

Heymsfield *et al.* (1991) examined two thin Ac clouds at about $-30°C$. They concluded that Ac clouds containing a convective structure are dynamically forced by radiative cooling effects. The radiative cooling causes sufficient negative buoyancy in cloud-top parcels to produce the observed downdraft velocities. They also pointed out that the absence of ice crystals implies a dearth of ice nuclei. Recently, Ryan (1996) noted that
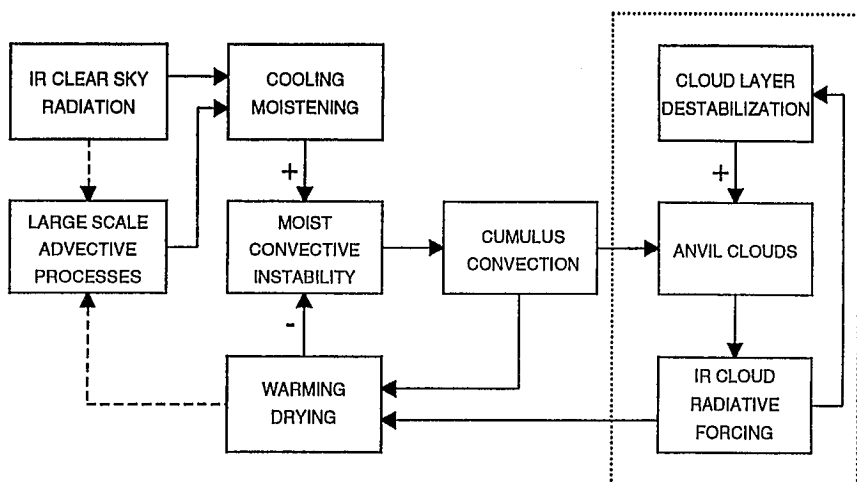
Figure 6 A schematic illustration of the mesoscale interactions of IR radiation and convection. The dashed lines indicate large-scale feedbacks that are not included in the CEM simulations. [From Fu *et al.* (1995). Reprinted with permission from the American Meteorological Society.]

observations indicate that middle-level stratiform clouds less than 1 km deep have either very few ice crystals or no ice crystals.

We studied the effects of radiation in simulated Ac cloud layers using the UCLA/UU CRM. We studied only liquid water clouds without precipitation because they represent most Ac cases. We also discussed the dynamics of the circulation occurring in the simulated Ac cloud layers. This study is described in more detail in Liu and Krueger (1997) and Liu (1998).

Starr and Cox (1985, hereafter SC85) simulated an Ac stratiformis cloud layer as a part of the same study in which they modeled a layer of cirrus. The profiles of temperature and moisture that we use are similar to those used by SC85 to simulate altocumulus. However, the initial supersaturation region thickness is reduced by one-half in our simulations. The model domain we used for our numerical simulations is 3.2 km long and 8.9 km high. The horizontal grid interval is 50 m. The vertical grid interval is 1 km from the surface to 5 km, 500 m from 5.0 to 5.5 km, and 25 m from 5.5 to 8.9 km.

Random perturbations are initially added to the potential temperature field in the supersaturation region to trigger the Ac circulations. The maximum magnitude of the perturbations is 0.1 K. The large-scale vertical velocity is zero.

We simulated a diurnal case which uses the radiative conditions at latitude 30°N on July 15. The starting time is midnight local time. The total simulation time is 36 hr. Solar radiation is significant between 6 and 18 hr, and after 29 hr.

In Fig. 7, the simulated field of liquid water mixing ratio (q_c) for the CRM simulation at 2 hr is displayed. This is a typical q_c snapshot for the simulation under nocturnal conditions. A cellular pattern is evident. The corresponding vertical velocity field is shown in Fig. 8. The updrafts are wider and weaker than the downdrafts. Comparison with Fig. 7 reveals
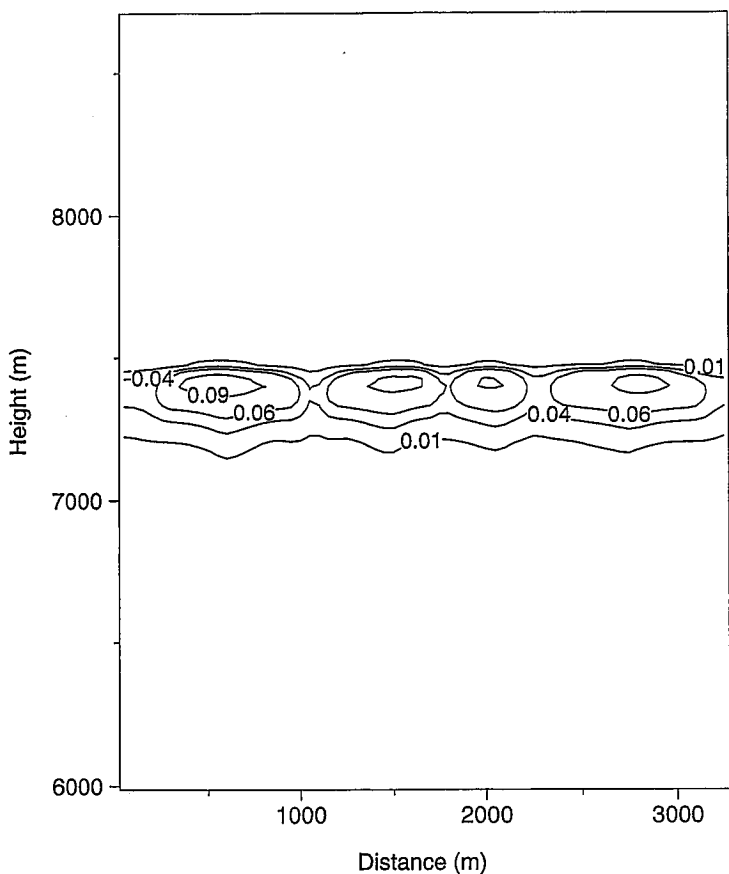
Figure 7 The liquid water mixing ratio field for the altocumulus cloud layer simulation at 2 hr.
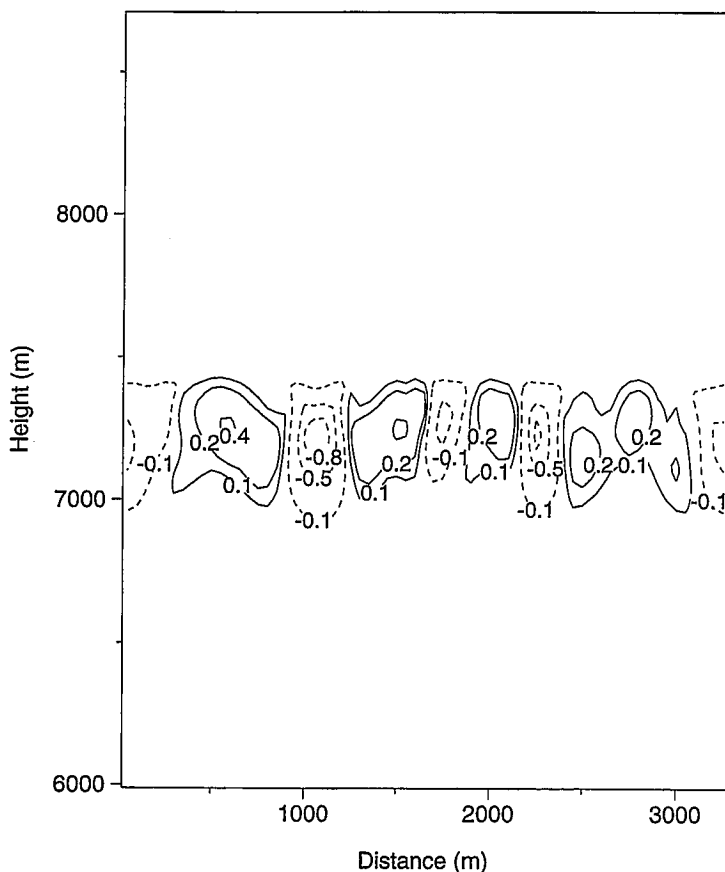
Figure 8   The vertical velocity field for the altocumulus cloud layer simulation at 2 hr.

that the updrafts are associated with regions of large q_c, and the downdrafts with regions of small q_c.

The evolution of the profiles of the horizontally averaged liquid water mixing ratio for the diurnal case is shown in Fig. 9. During the night, the cloud layer ascends and the cloud depth is almost constant. During the daytime, the cloud top height is nearly constant and the cloud depth decreases. After sunset, the cloud depth increases and the cloud layer again ascends. A decreased cloud depth during the daytime under diurnal conditions also occurred in the stratocumulus simulations of Bougeault (1985), Turton and Nicholls (1987), and Wyant *et al.* (1997), and in the marine stratocumulus observations of Hignett (1991).

The effects of radiation on the Ac layer depend on the radiative heating rate profile within the cloud layer. Figure 10 shows the evolution of the horizontally averaged total radiative heating rate for the diurnal case. During the night, there is strong cooling in the upper part of the cloud layer, and some heating in the lower part of the cloud layer. During the morning, we find that the maximum solar heating and IR cooling rates both occur near the cloud top, just like in a simulation of a stratocumulus-topped boundary layer under diurnal conditions (Krueger *et al.*, 1995b). In
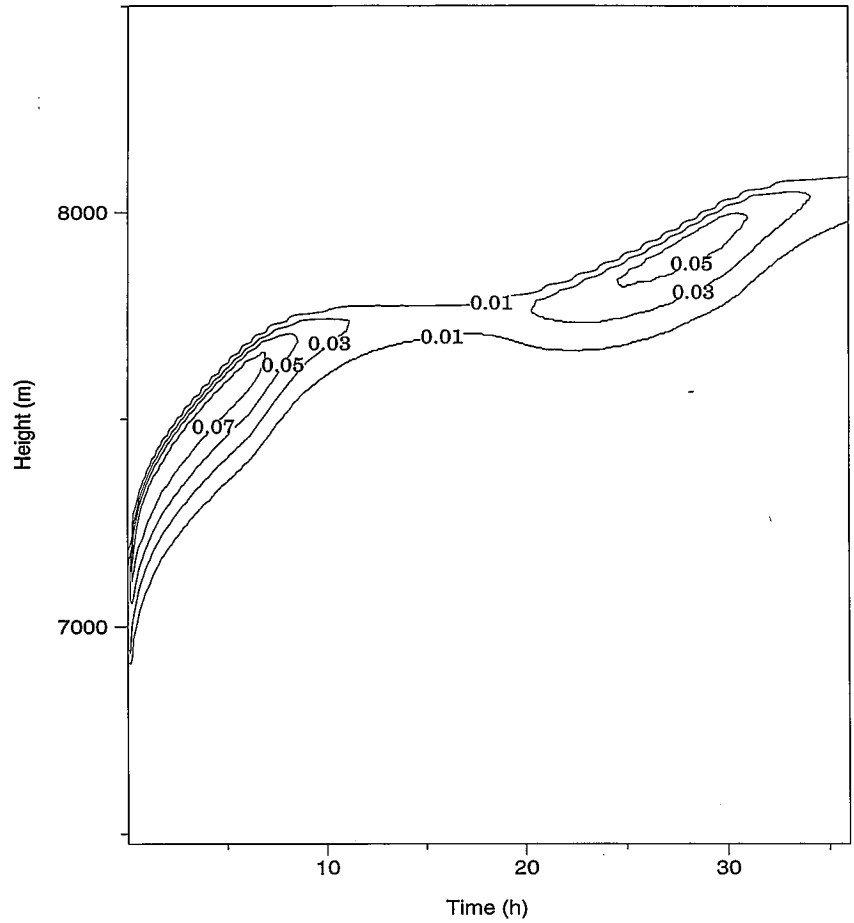
Figure 9 Time–height plot of the horizontally averaged liquid water mixing ratio for the altocumulus cloud layer simulation.
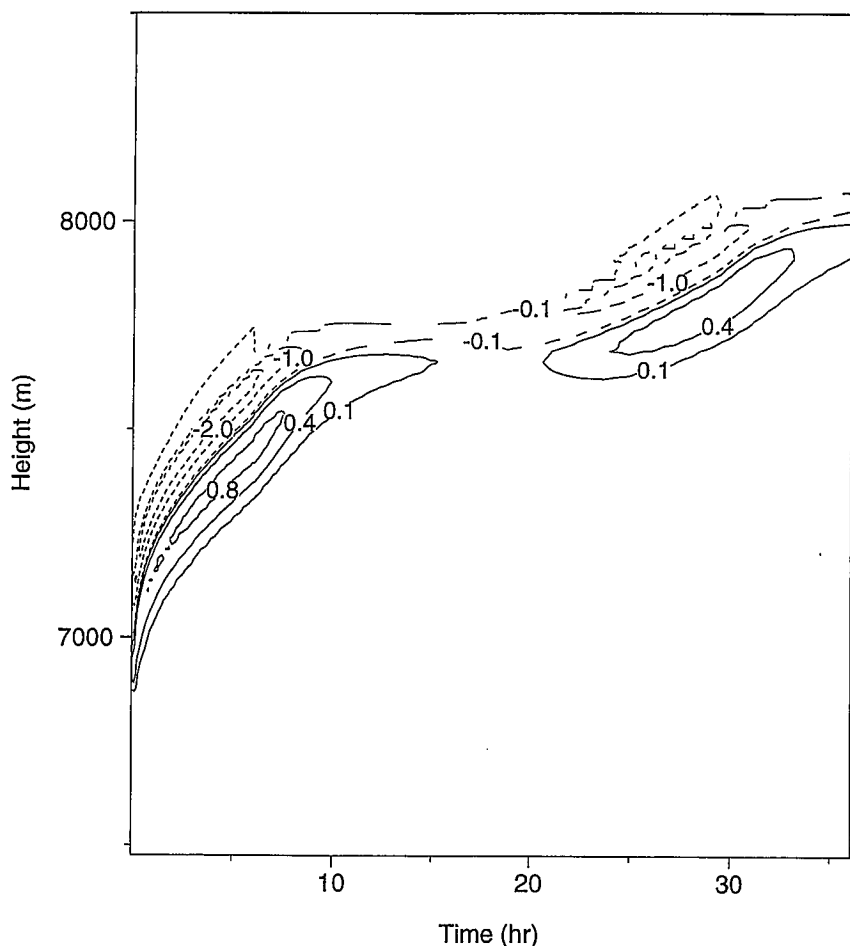
Figure 10   Time–height plot of the horizontally averaged total radiative heating rate for the altocumulus cloud layer simulation.

the Ac layer, this pattern produces net heating in most of the cloud layer during the morning, which decreases the cloud depth and cloud water mixing ratio. By the late afternoon, the cloud region is almost entirely radiatively cooling although the cooling rate is very small, which agrees with the thin afternoon Ac cloud examined by Heymsfield *et al.* (1991).

In Fig. 11 the profiles of the 6-hr averaged updraft and downdraft vertical velocities are shown for the diurnal case. The diurnal variation is obvious. The updraft and downdraft profile shapes are quite similar.

However, the downdraft peak values are larger. In the stratocumulus-topped boundary layer cases simulated by Krueger *et al.* (1995c) and Moeng *et al.* (1992), the updraft and downdraft profile shapes are also quite similar, but they have almost the same peak magnitudes.

The Ac cloud layer thickness and LWP (liquid water path) are controlled by the net cloud layer radiative heating and entrainment warming and drying. A positive feedback exists between LWP and IR radiative cooling, whereas a negative feedback exists between LWP and solar radiative heating. Typically, a negative feedback also exists between LWP and entrainment, but this depends on the relative humidity of the air above cloud top (Randall, 1984).

At the beginning of the diurnal simulation, the IR radiative cooling is large in the upper part of the Ac layer (Fig. 10). This quickly produces an active cloud layer circulation (Fig. 11) and a large entrainment rate (equal to the cloud top ascent rate in these simulations; see Fig. 9). But entrainment has a weak negative feedback on IR radiative cooling in this case. Therefore, only after several hours does the Ac structure and circulation become nearly steady.

After sunrise in the diurnal simulation, solar radiative heating cancels most of the IR radiative cooling in the upper part of the Ac layer, which means that the radiative destabilization is greatly reduced. The dramatic
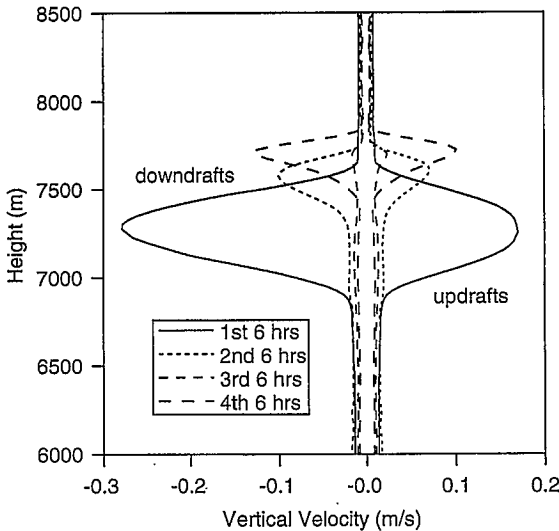

Figure 11 The profiles of the 6-hr-averaged updraft and downdraft vertical velocities for the altocumulus cloud layer simulation.

effect of this on the cloud layer circulation is shown in Fig. 11 and on the entrainment rate in Fig. 9. Solar radiation produces overall cloud layer heating during the morning (Fig. 10), which decreases the cloud depth and cloud water mixing ratio (Fig. 9). Both solar radiative heating and IR radiative cooling in the upper part of the Ac layer decrease quickly as the cloud thins. After most of the cloud liquid water has evaporated, IR cooling balances solar heating so that near-zero total radiative heating exists (Figs. 9 and 10). This allows the cloud to be maintained during the remainder of the afternoon. After sunset, the net cooling increases and the cloud water mixing ratio increases through the night (Fig. 9). At the same time, radiative destabilization increases and as a result so does the cloud circulation and the entrainment rate (Figs. 9 and 11).

These results suggest that actual Ac layers should display a diurnal variation in thickness. It is likely that some Ac layers will completely disappear during the day, and other Ac layers may simply become broken or scattered. Lazarus *et al.* (2000) examined the diurnal variation of Ac cloud amount over the southern Great Plains based on 10 years of edited synoptic cloud reports. They found a significant diurnal variation during the spring, summer, and fall, with maximum cloud amounts at 0600 local standard time and minimum amounts at 1800 local standard time. During winter there was no detectable diurnal variation. These observations are consistent with the CRM results.

IV. STRATOCUMULUS-TO-TRADE CUMULUS TRANSITION IN THE SUBTROPICAL MARINE BOUNDARY LAYER

In the eastern and equatorward quadrants of the subtropical high-pressure zones, the low level air flow (or trajectory) is generally equatorward and westward, across a progressively warmer sea surface and into regions of decreased subsidence. As air flows equatorward over the subtropical oceans, the initially stratocumulus-topped boundary layer (STBL) evolves into a trade cumulus boundary layer (TCBL). This stratocumulus-to-cumulus transition (SCT) involves both a radical decrease in cloud amount, from overcast stratocumulus to scattered cumulus, and a change in the boundary-layer structure and circulation from a well-mixed STBL to a two-layer TCBL with a well-mixed subcloud layer and a conditionally unstable cloud layer.

The physical processes responsible for the SCT have long been a puzzle. Randall (1980) and Deardorff (1980) suggested that cloud-top entrainment

instability (CEI) is responsible for the SCT. They hypothesized that under certain conditions, entrainment leads to the generation of turbulence kinetic energy in a stratocumulus layer, which in turn leads to further entrainment and eventual breakup of the cloud layer. This process depends on rapid mixing and evaporative cooling of the entrained air.

However, subsequent observational studies found that STBLs occurred where the stratocumulus layers were predicted to break up due to CEI. More recent theoretical studies (e.g., Krueger, 1993) suggest that CEI does not occur as originally conceived because mixing of entrained air and cloudy air does not proceed rapidly enough.

The first attempts to model the SCT used versions of Lilly's (1968) cloud-topped, mixed-layer model. Schubert *et al.* (1979) presented solutions of a horizontally inhomogeneous version. In one of their experiments, boundary-layer air flows through regions of constant large-scale divergence but increasing SST. The parameters chosen were typical of the eastern North Pacific in July. In this experiment, the boundary layer warms, moistens, and deepens with time, and the turbulent fluxes increase. Wakefield and Schubert (1981) integrated the same model along climatological trajectories in the eastern North Pacific. This "Lagrangian" approach involves translating the model along the boundary-layer trajectory at a rate equal to the observed surface wind speed, while the lower and upper boundary conditions are continuously adjusted to their observed values along the trajectory. In neither of these studies was it possible to simulate the transition from a STBL to a TCBL because the boundary-layer model assumes that a mixed-layer structure always exists.

Moeng and Arakawa (1980) used 1-D second-moment turbulence closure, but in the framework of a 2-D (y-z) mesoscale model with a horizontal domain of 1000 km and a horizontal grid interval of 10 km. The flow field within the model domain was that of the downward and equatorward branch of a Hadley cell. They found that the uniform stratus cloud layer was destroyed on the equatorward side of the domain, producing a mesoscale circulation of 30–50 km in size.

These studies of the SCT used 1-D approaches to represent the boundary-layer turbulence. The major drawback to using such approaches for simulating the SCT is their inability to predict the cloud fraction accurately. Most if not all 1-D models must be tuned for each type of boundary-layer cloudiness regime. In particular, boundary layers containing cumulus clouds are difficult to model using any 1-D turbulence closure, since the standard closure assumptions assume that the turbulence is nearly isotropic and nearly Gaussian. Cumulus convection has a large vertical velocity skewness and is thus highly non-Gaussian.

In 1-D bulk or turbulence closure models, the convective circulations and the small-scale turbulence are both parameterized. In contrast, a 3-D LES explicitly simulates the convective circulations. Only the small, sub-grid-scale eddies are parameterized. LES models have successfully simulated the STBL and the TCBL (e.g., Moeng, 1986; Sommeria, 1976; Siebesma and Cuijpers, 1995); however, LES models are too computationally expensive to use for the multiday simulations required to study the SCT.

To overcome the limitations of the 1-D and 3-D approaches, we used a 2-D (*x-z*) numerical model, the UCLA/UU CRM, to simulate the SCT (Krueger *et al.*, 1995b). For simulating the SCT, a 2-D CRM offers the best combination of generality and economy in comparison to 1-D models and 3-D LES models. A 2-D CRM does not require the cloud-regime-specific input that 1-D models do, and is much less computationally expensive than LES models. Soong and Ogura (1980) were the first to use this type of model to simulate the TCBL.

We used the Lagrangian approach for our SCT simulations, which involves translating the domain along the boundary-layer trajectory at a rate equal to boundary-layer wind speed. This allows the CRM's domain to be small enough to allow high spatial resolution at a moderate computational expense. With this spatial resolution, the CRM can explicitly represent large convective boundary layer eddies. Turbulence other than the large eddies is parameterized using a third-moment turbulence closure. As in the Lagrangian studies described above, we used a July climatological boundary layer trajectory over the northeastern Pacific southwest of California.

We performed two simulations, SCT_1 and SCT_2. The boundary conditions and large-scale forcing are based on the climatological data presented by Betts *et al.* (1992). The surface wind speed was 7 m/s, the divergence was 3×10^{-6} s^{-1}, and the initial SST was 290.2 K. The SST increased 1.8 K/day along the trajectory.

These simulations did not include drizzle, the diurnal cycle, large-scale divergence changes, or mesoscale circulations. Each of these processes has been proposed as a necessary ingredient for a SCT. If a realistic SCT can occur in the simulations in the absence of these processes, it would suggest that these processes are not essential.

For these two simulations, the domain was 4.8 km wide and the horizontal grid size was 75 m. It is not possible to simulate mesoscale circulations with this horizontal domain size. In SCT_1, the domain was 2 km high and the vertical grid size was 50 m, whereas in SCT_2, the domain was 3 km high and the vertical grid size was 75 m.

In SCT_1, the boundary layer was initialized as a cloud-topped mixed layer in equilibrium with a SST of 290.2 K. This case was run for 120 hr. SCT_2 was run because the boundary layer's growth in SCT_1 was significantly affected by the top of the domain after about 84 hr. In SCT_2, the boundary layer was initialized with the SST and horizontally averaged profiles of potential temperature, water vapor mixing ratio, and liquid water mixing ratio of SCT_1 at 69 hr. This case was run for 75 hr (i.e., until hour 144 relative to the start of SCT_1).

The CRM included an advanced solar and infrared radiation code for these simulations (Krueger et al., 1995b). The solar radiation was diurnally averaged so there was no diurnal cycle in the numerical simulation. The solar zenith angle (51.8°) was the mean *daytime* solar zenith angle for mid-July at 30°N.

The horizontally averaged cloud fraction versus height and time is shown in Fig. 12. The transition from overcast to broken and finally scattered clouds is evident. The cloud cover decreases from 100% at the start to about 20% at the end of 6 days. The results presented in Fig. 12 agree with the decrease in cloud cover observed along the climatological trajectory over increasing SST (Betts et al., 1992). The simulated cloud top and base levels are also similar to those observed (as reported by Betts et al., 1992). Riehl et al. (1951) presented the first set of soundings along the climatological trade wind trajectory northeast of Hawaii, which corre-
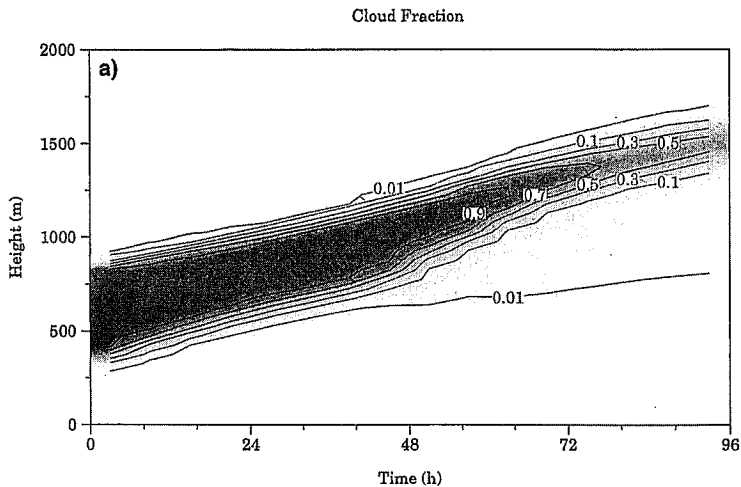

Cloud Fraction

Figure 12 Horizontally averaged cloud fraction for (a) SCT_1 and (b) SCT_2. [From Krueger et al. (1995b). Reprinted with permission from the American Meteorological Society.]
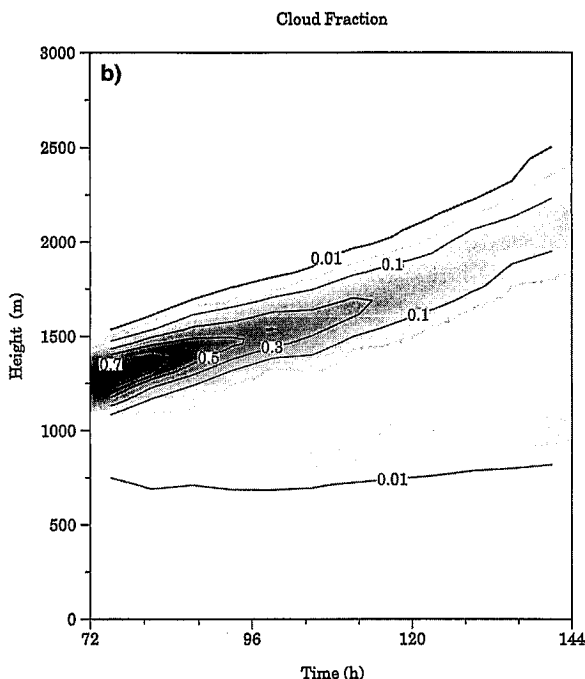
Cloud Fraction

Figure 12   (*Continued*)

sponds to days 4–6 of SCT_2. Riehl *et al.* found that the cloud base slowly rises, while the inversion base rises from 900 to 800 mb, and inversion top from about 800 to 730 mb, in general agreement with Betts *et al.* (1992) and simulation SCT_2.

Examination of the 2-D cloud fields during SCT_1 (shown in Krueger *et al.*, 1995b) reveals that at 24 hr, the boundary layer is stratocumulus topped. By 48 hr, the stratocumulus-topped boundary layer has deepened significantly and some cumulus clouds are forming below it. At 72 hr, cumulus clouds are rising into a broken stratocumulus layer. This cumulus-under-stratocumulus cloud regime (WMO cloud type $C_L 8$) is commonly observed at the location of Weather Ship N (30°N 140°W) during the summer (Klein *et al.*, 1994). The July average SST at Ship N is 295 K, which corresponds to hour 65 of SCT_1. After 72 hr in SCT_1 and SCT_2, the stratocumulus layer becomes less persistent, and by 120 hr, it occurs only in association with detraining cumulus clouds.

The 2-D velocity fields (shown in Krueger *et al.*, 1995b) portray the circulation changes during the SCT. At 24 hr, large eddies extend from the surface to cloud top. At 48 hr, some separation ("decoupling") between

cloud and subcloud layer circulations is evident. At 72 hr, in the Cu-under-Sc regime, most of the eddies no longer extend through the entire boundary layer. This two-layer circulation pattern becomes progressively more evident as the stratiform cloud layer thins and breaks up, leaving only scattered cumulus clouds by 120 hr. The transition in the *circulation* pattern from a one-layer to a two-layer structure precedes the transition in the *cloud* pattern from overcast to scattered by 2–3 days. These changes in the boundary-layer circulation are associated with significant changes in the thermodynamic structure.

Figure 13 contains sequences of the horizontally averaged profiles of liquid water mixing ratio (q_c), total water mixing ratio (q_w), and liquid water static energy (s_l). Each sequence spans the entire 6 days of the two simulations. Days 0–3 are from SCT_1, and days 4–6 are from SCT_2. The simulated profiles of s_l and q_w, plus cloud base and cloud top height, are in generally good agreement with observations made during field studies of the trade cumulus boundary layer and the stratocumulus-topped boundary layer.

The q_c profiles (Fig. 13a) show that during the first 2 days, only an overcast stratocumulus cloud layer exists. After 2 days, a layer containing scattered cumulus clouds and very small q_c develops below the stratocumulus layer.

Figures 13b and 13c show the q_w and s_l profiles. Both q_w and s_l are conserved during moist adiabatic processes, and so their profiles are uniform with height in a mixed layer. During the first two days, both quantities exhibit mixed-layer profiles. Observations of the STBL indicate a mixed-layer structure capped by a strong temperature inversion and rapid decrease in water vapor mixing ratio in agreement with the simulation. Klein *et al.* (1994) present average July soundings at Weather Ship N where the Cu-under-Sc regime is commonly observed. These soundings do not exhibit a mixed-layer structure, in agreement with the corresponding simulation profiles at day 3.

By day 4, a two-layer structure resembling that of the TCBL has developed. Radiosonde soundings of the TCBL often exhibit a multilayer structure consisting of a mixed layer capped by an isothermal transition layer about 100 m thick in which the mixing ratio decreases. Above the transition layer, the conditionally unstable cloud layer extends to the base of the trade inversion. The mixing ratio decreases upward in the cloud layer. In the trade inversion, which caps the cloud layer, the temperature increases, and the mixing ratio decreases rapidly. The profiles for days 5 and 6 exhibit a mixed layer below the base of the cumulus clouds. Above a transition zone at about 750 m there is a stratified cloud layer. Due to averaging, the transition zone is not well defined. Across the transition
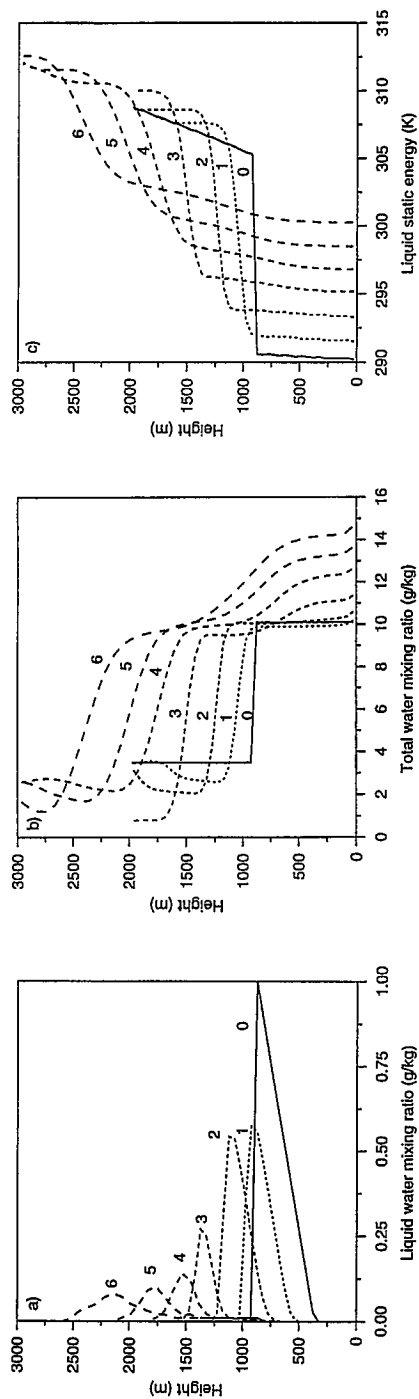
Figure 13 Horizontally averaged (a) liquid water mixing ratio, (b) total water mixing ratio, and (c) liquid water static energy at 1-day intervals for SCT_1 (days 0–3) and SCT_2 (days 4–6). [From Krueger *et al.* (1995b). Reprinted with permission from the American Meteorological Society.]

zone, q_w drops rapidly. Interestingly, the upper part of the cloud layer that contains the stratocumulus layer (see Fig. 13a) is relatively well-mixed in q_w. This feature may be the result of convective motions generated by cloud-top radiative and evaporative cooling that are restricted to the stratocumulus layer.

Figure 13c shows, as also found by Riehl *et al.* (1951), that the cloud layer stratification increases downstream in the trade wind region (days 4–6), while the inversion strength decreases.

Overall, the simulated SCT resembles observations. As noted previously, drizzle, the diurnal cycle, large-scale divergence changes, and mesoscale circulations were not included in the simulation, which therefore demonstrates that these processes are not essential for a SCT.

The results also suggest that there are three stages in the transition from the stratocumulus-topped boundary layer (STBL) to the trade cumulus boundary layer (TCBL). The simulated transition involves an intermediate stage, the "cumulus-under-stratocumulus" boundary layer (CUSBL). The CUSBL has a two-layer structure, like the TCBL, with a well-mixed subcloud layer and a stratified (partly mixed) cloud layer. The transition to a typical TCBL structure preceded the transition to a typical TCBL cloud fraction by about 2 days.

Krueger *et al.* (1995c) developed a convective updraft/downdraft partitioning scheme based on trajectory analysis and used it to analyze the boundary-layer circulation changes during the simulated SCT. They found that the "cumulus-under-stratocumulus" boundary layer, like the trade cumulus boundary layer, has an active subcloud layer circulation that is linked to the cloud layer by narrow cumulus updrafts. The circulation analysis also revealed that during the SCT, convective downdrafts originating near cloud top due to cloud-top cooling became less important, while convective (cumulus) updrafts became more important. This suggests that cloud-top entrainment instability does not play a significant role in the SCT.

A. Decoupling

The development of the CUSBL from the well-mixed STBL is due to the increasing frequency of "decoupling" of the subcloud and cloud layers. During decoupling, turbulent eddies are limited to the separate layers. Intermittent coupling of the two layers is achieved by cumulus convection. Decoupling and coupling are illustrated in Fig. 14, which shows a time series from SCT_1 of the horizontally averaged total water mixing ratio at two levels, one in the middle of the subcloud layer, and the other in the upper cloud layer. During decoupling, the subcloud layer is moistened by
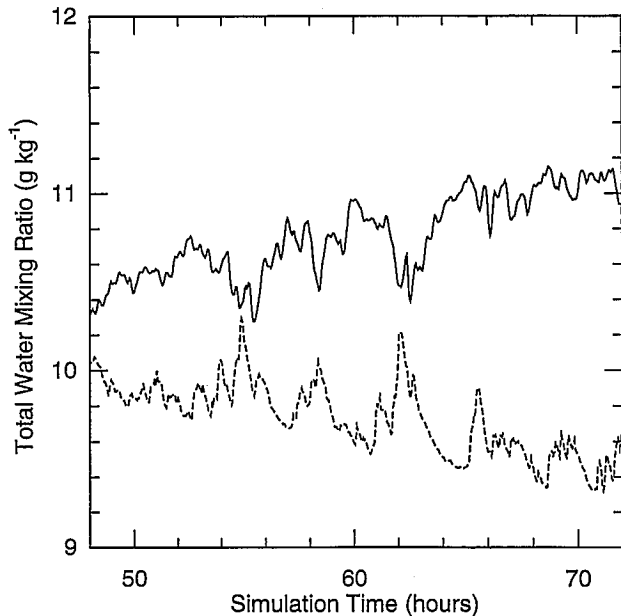
Figure 14   Time series from SCT_1 of the horizontally averaged total water mixing ratio in the middle of the subcloud layer (solid) and in the upper cloud layer (dashed).

surface fluxes while the upper cloud layer is dried by entrainment. During coupling, the opposite occurs, as cumulus updrafts carry moist subcloud-layer air into the cloud layer, while cumulus downdrafts and entrainment at the top of the subcloud layer transport dry air from the cloud layer into the subcloud layer.

Decoupling occurs when cloud-layer downdrafts are unable to penetrate to the surface due to deepening of the boundary layer. Recoupling occurs in the form of cumulus updrafts once the convective available potential energy of subcloud layer parcels increases sufficiently. This increase is due to surface fluxes that increase the moist static energy of the subcloud layer, and to radiative and evaporative cooling of the cloud layer.

Wyant *et al.* (1997) also studied the stratocumulus-to-trade cumulus transition using a similar numerical modeling approach, whereas Brether-ton and Wyant (1997) examined the process of decoupling.

B. SUMMARY

To simulate the stratocumulus-to-trade cumulus transition (SCT), a model must be able to represent a cumulus-under-stratocumulus cloud

regime. A mixed-layer model can, at most, predict the onset of such a regime (by diagnosing decoupling). To be capable of simulating SCT, a 1-D turbulence closure model must include a realistic parameterization of cloud fraction and the associated buoyancy fluxes. Because a 2-D CRM explicitly represents the large convective eddies associated with cloud formation, it should not require the cloud-regime-specific input that 1-D models do. The results of 2-D CRM simulations of the SCT suggest that this is indeed the case.

V. ENHANCEMENT OF SURFACE FLUXES BY TROPICAL CONVECTION

Large-scale models typically diagnose the surface turbulent fluxes of sensible and latent heat over the ocean using the large-scale (i.e., area-averaged) near-surface temperature and water vapor mixing ratio and the speed of the large-scale wind vector. These fluxes may be called the "vector-mean" surface fluxes. Esbensen and McPhaden (1996) defined "mesoscale enhancement" as the difference between the vector-mean surface fluxes and the actual large-scale surface fluxes. In the absence of mesoscale circulations, there would be no mesoscale enhancement.

Based on buoy data, Esbensen and McPhaden (1996) found that mesoscale enhancement of evaporation can reach 30% of the total evaporation. They also showed that mesoscale enhancement is primarily due to mesoscale wind variability ("gustiness") and is associated with periods of significant precipitation.

Several multiday, large-domain simulations of tropical maritime convection were performed with the 2-D UCLA/UU CRM, as reported by Xu *et al.* (1992). Analyses of these simulations indicate that the characteristics of mesoscale enhancement as simulated by the model are quite similar to those observed (Zulauf and Krueger, 1997, 2000).

In the CRM, the bulk aerodynamic method of Deardorff (1972) is used to calculate the local (i.e., grid-point) latent and sensible heat fluxes at the surface, E and S. Using the notation of Esbensen and McPhaden (1996), the domain-averaged latent heat flux, $\langle E \rangle$, for example, is then

$$\langle E \rangle = \rho L_v \langle C_q(U, \cdot)U(q_s - q) \rangle,$$

where ρ is the density, L_v is the latent heat of vaporization, C_q is the stability-dependent transfer coefficient, U is the wind speed, $\cdot$ represents additional dependences of C_q, q_s is the surface mixing ratio, q is the near-surface mixing ratio, and angle brackets indicate the domain average.

The corresponding vector-mean flux is

$$E_{\mathrm{v}} = \rho L_{\mathrm{v}} C_{\mathrm{q}}(V, \langle \cdot \rangle) V(\langle q_{\mathrm{sfc}} \rangle - \langle q \rangle),$$

where V is the magnitude of the average (or resultant) wind vector, which is predicted by large-scale models. By replacing V with the domain-averaged wind speed, $\langle U \rangle$, we obtain the scalar-mean flux,

$$E_{\mathrm{s}} = \rho L_{\mathrm{v}} C_{\mathrm{q}}(\langle U \rangle, \langle \cdot \rangle) \langle U \rangle (\langle q_s \rangle - \langle q \rangle).$$

In the CRM simulations, the differences between V and $\langle U \rangle$ can be significant. We used V and $\langle U \rangle$ to calculate the vector-mean and scalar-mean latent and sensible heat fluxes, and compared them with the domain-averaged fluxes. We found that the vector-mean fluxes do a poor job of estimating the domain-averaged fluxes (i.e., that the mesoscale enhancement in the simulations is significant), but the scalar-mean fluxes track them extremely well.

For example, in one 11-day simulation (Q03), $\langle E \rangle = 88.2$ W m^{-2} and $E_{\mathrm{v}} = 57.4$ W m^{-2}, whereas $E_{\mathrm{s}} = 90.5$ W m^{-2}. The results are similar for the sensible heat fluxes: $\langle S \rangle = 17.5$ W m^{-2} and $S_{\mathrm{v}} = 11.1$ W m^{-2}, whereas $S_{\mathrm{s}} = 17.7$ W m^{-2}. The rms errors of the vector-mean and scalar-mean fluxes (relative to the domain-averaged fluxes) are 33.4 and 2.4 W m^{-2} for E_{v} and E_{s}, and 6.9 and 0.4 W m^{-2} for S_{v} and S_{s}, respectively. These are nearly the same as the mean errors.

We can approximate the scalar-mean fluxes, which are good estimates of the large-scale (i.e., domain-averaged) fluxes, if we can parameterize $\langle U \rangle$ in terms of V. Because V is always less than or equal to $\langle U \rangle$, we may introduce a gustiness speed U_{g} such that

$$\langle U \rangle^2 = V^2 + U_{\mathrm{g}}^2.$$

The gustiness speed represents the contribution to the average wind speed from sub-grid-scale circulations (e.g., Mahrt and Sun, 1995). We will assume that U_{g} is primarily due to circulations driven by cumulus convection. However, boundary-layer convection also contributes to U_{g}, and formulations to parameterize this component of the gustiness speed have already been developed (e.g., Beljaars, 1995). (The CRM includes one.) Therefore, we separate U_{g} into components due to boundary layer convection, $U_{\mathrm{g,BL}}$, and due to cumulus convection, $U_{\mathrm{g,CU}}$, so that

$$\langle U \rangle^2 = V^2 + U_{\mathrm{g,BL}}^2 + U_{\mathrm{g,CU}}^2.$$

The variance of the cumulus-scale horizontal wind vector,

$$U_{\sigma,\mathrm{CU}}^2 \equiv \langle u_{\mathrm{CU}}'^2 \rangle + \langle v_{\mathrm{CU}}'^2 \rangle,$$

where u'_{CU} and v'_{CU} are the cumulus-scale deviations from $\langle u \rangle$ and $\langle v \rangle$, the components of the average (or large-scale) wind vector, can be formally related to the gustiness speed due to cumulus convection:

$$U_{g,CU} = \alpha U_{\sigma,CU}.$$

Theoretical methods give a value of 0.8 for α (Jabouille *et al.*, 1996). In our simulations, α is usually between 0.75 and 0.85. These results suggest that a constant value of α is a good approximation. Then $U_{g,CU}$, and hence $\langle U \rangle$, can be obtained if $U_{\sigma,CU}$ can be parameterized.

The quantity $U_{\sigma,CU}^2$ should be related to a measure of the intensity of the cumulus convection, such as the updraft cloud mass flux at cloud-base level. The scatter plots in Fig. 15 show how $U_{\sigma,CU}^2$ is related to various measures of cumulus activity based on the results of several multiday CEM simulations. The quantities in the plots are 3-hr domain (512-km) averages. It is interesting that all six measures chosen are about equally correlated with $U_{\sigma,CU}^2$. In particular, the surface rainfall rate is as well correlated as any of the other more direct measures of cumulus activity. Jabouille *et al.* (1996) used observations to develop a similar parameterization based on the surface rainfall rate.

The linear fits displayed in Fig. 15 form the basis of a parameterization of $\langle U \rangle$ that augments V with a gustiness speed due to cumulus convection, which in turn can be linked via $U_{\sigma,CU}^2$ to one of several measures of cumulus activity. Many of these measures are available in large-scale models.

VI. PLUMES GENERATED BY ARCTIC LEADS

The interactions between sea ice, open ocean, atmospheric radiation, and clouds over the Arctic Ocean exert a strong influence on global climate. Uncertainties in the formulation of interactive air–sea–ice processes in global climate models (GCMs) result in large differences between the Arctic and global climates simulated by different models. In particular, the effects of leads on the atmosphere and the surface heat budget of the Arctic Ocean must be more accurately represented in climate models to allow possible feedbacks between leads and the sea ice thickness.

We are using the UCLA/UU Cloud Resolving Model to increase our understanding of (1) how atmospheric convective plumes emanating from leads affect the large-scale atmospheric budgets of sensible heat, water vapor, and condensate, and (2) how the contribution by such plumes to Arctic cloud cover, directly through the production of clouds and indirectly by increasing boundary-layer moisture, affects the surface heat budget of the Arctic Ocean.
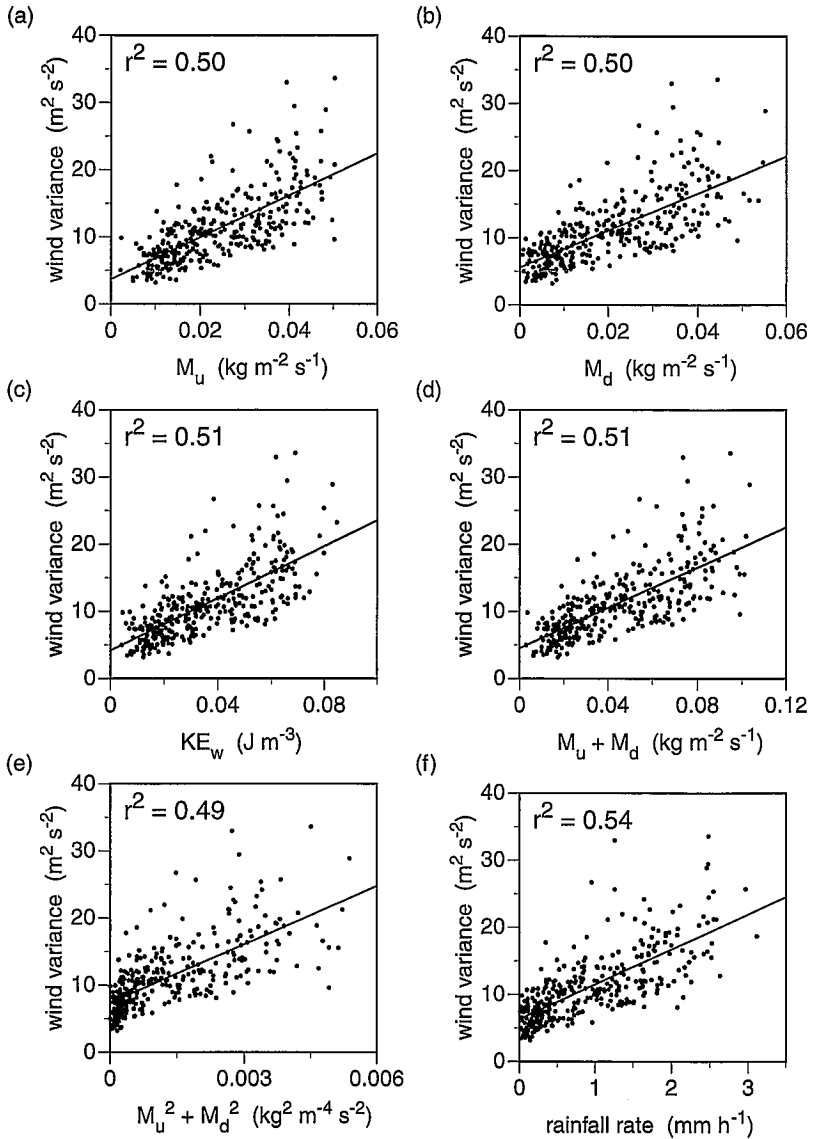
Figure 15   Scatterplots of large-scale cumulus activity versus $U^2_{\sigma,CU}$ using consensus data for (a) updraft cloud mass flux $\langle M_u \rangle$, (b) downdraft cloud mass flux $\langle M_d \rangle$, (c) vertical component of kinetic energy $\langle KE_w \rangle$, (d) $\langle M_u \rangle + \langle M_d \rangle$, (e) $\langle M_u^2 \rangle + \langle M_d^2 \rangle$, and (f) surface precipitation rate $\langle P \rangle$. Also shown for each scatterplot is the least squares linear fit and r^2, the coefficient of determination.

Glendening and Burk (1992) and Glendening (1994) performed 3-D large-eddy simulations of the convective plumes generated by 200-m-wide leads with different geostrophic wind angles. We performed 2-D CRM simulations of the same cases to gauge the impacts of differences in model physics (Zulauf and Krueger, 1999).

The cases are characterized by specified ocean ($-2°C$) and ice ($-29°C$) temperatures, a stable, nearly isothermal, lower troposphere, a surface temperature of $-27°C$, and a geostrophic wind speed of 2.5 m s^{-1}. The CRM's vertical grid size was 4 m, and the horizontal grid size was 8 m. Each simulation was for 14 min.

Table III describes the setup of each of the four cases and summarizes the simulation results. Cases A, B, and C differ only in the geostrophic wind angle, and cases A and D differ only in the lead width.

Cases A, B, and C correspond to three of Glendening's cases. Figure 16 shows the time-averaged total turbulent kinetic energy for these cases. As found by Glendening, the plume character greatly depends on the geostrophic wind angle. For a geostrophic wind angle of 0 deg (case A), the geostrophic wind is parallel to the lead. For this case, the turbulent plume is symmetrical, erect, concentrated above the center of the lead, and reaches a height of 190 m. For a geostrophic wind angle of 15 deg (case B), the plume rises from the lee side of the lead. Further downstream it becomes elevated and reaches its maximum height of 115 m. For a geostrophic wind angle of 90 deg (case C), the geostrophic wind is perpendicular to the lead. For this case, the turbulent plume is similar to that for an angle of 15 deg, but the plume reaches only 65 m, and does not become completely detached from the surface.

The plume characteristics simulated by the 2-D CRM are qualitatively similar to those of Glendening's 3-D large-eddy simulations. The dependence of the plume height on geostrophic wind angle is in quantitative agreement with Glendening's results.

Due to the computational requirements of large-eddy simulations, Glendening was not able to study the dependence of plume characteristics

Table III
Simulations of Arctic Leads

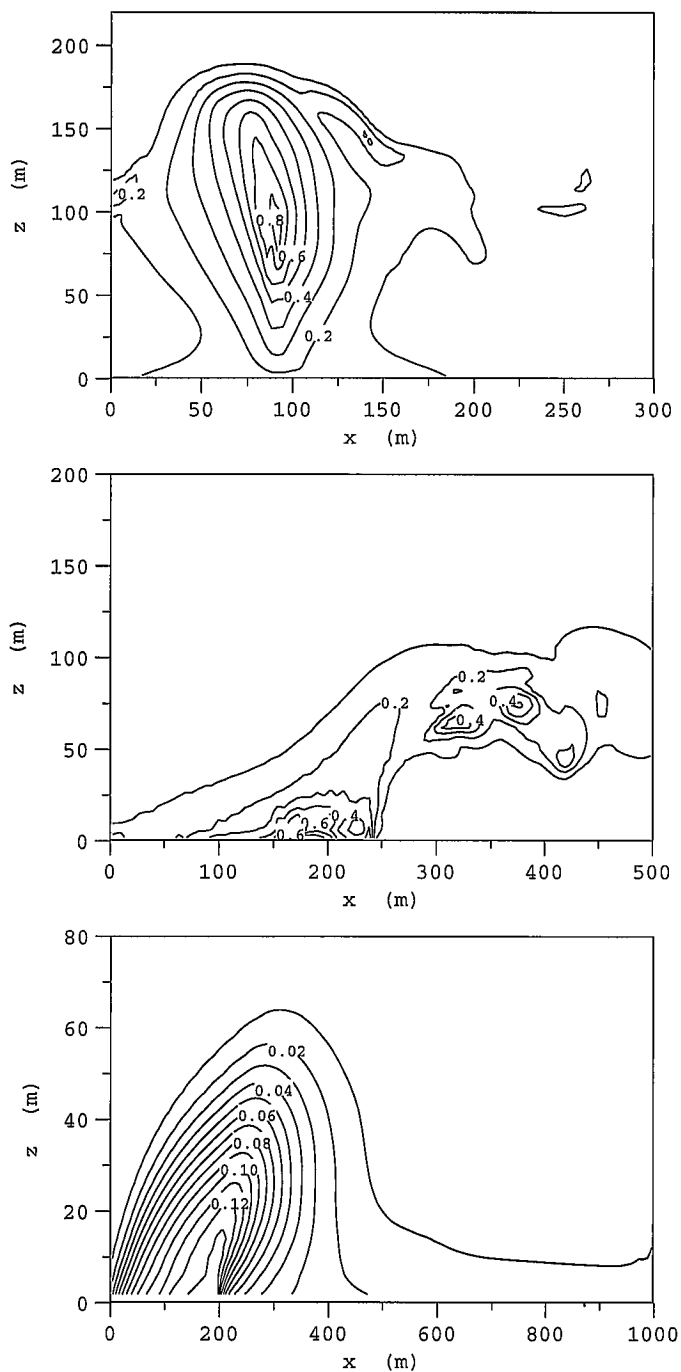| Case	Domain size (m)	Lead width (m)	Geostrophic wind angle (deg)	$(F_s)_{lead}$ (W m^{-2})	$(LF_q)_{lead}$ (W m^{-2})	Plume height (m)
A	768	200	0	244	73	190
B	768	200	15	246	75	115
C	2304	200	90	243	72	65
D	768	400	0	264	80	270

Figure 16   Mean total turbulent kinetic energy (m^2 s^{-2}) for cases A (top), B (middle), and C (bottom).

on lead width. However, it is possible to use a 2-D CRM to study this dependence in detail because such models are relatively economical. Table III shows that with a lead-parallel geostrophic wind, a plume generated by a 400-m-wide lead (case D) reaches 270 m, whereas one generated by a 200-m-wide lead (case A) reaches 190 m. The dependence on lead width is significant.

It would be interesting to use the 2-D CRM to study how cloud formation and interactive radiation affect the plume characteristics, and how cloudiness from a plume evolves and affects the radiative fluxes at the surface.

VII. CONCLUSIONS

Cloud-resolving models are numerical models that explicitly represent the cloud-scale circulations and their interactions with microphysical, radiative, and small-scale turbulent processes. Most CRMs are 2-D models, which allows them to simulate the mesoscale organization of cloud systems over multiday time periods. In contrast, 3-D large-eddy simulation models are limited to simulating large turbulent eddies over periods of several hours, and 1-D column models must parameterize the cloud-scale circulations, as well as the turbulence.

Two-dimensional CRMs have been used to study a variety of cloud types and systems, as this chapter illustrates. During the next decade, we can expect a number of improvements in CRMs. New observations of clouds will allow more thorough evaluations of the microphysical and radiative transfer parameterizations employed in CRMs. In addition, ever-increasing computational resources will allow 3-D CRMs and very-large-domain 2-D CRMs to become more commonly used. In the not-so-distant future, 3-D CRMs with domains covering an entire large-scale disturbance will become reality. This will allow cloud-resolving simulations of the interaction between cumulus ensembles and the large-scale circulation.

ACKNOWLEDGMENTS

REFERENCES

Beljaars, A. C. M. (1995). The parameterization of surface fluxes in large scale models under free convection. *Quart. J. Roy. Meteor. Soc.* **121,** 255–270.

Betts, A. K., P. Minnis, W. Ridgway, and D. F. Young (1992). Integration of satellite and surface data using a radiative-convective oceanic boundary-layer model. *J. Appl. Meteor.* **31**, 340–350.

Bougeault, P. (1985). The diurnal cycle of the marine stratocumulus layer: A higher-order model study. *J. Atmos. Sci.* **42**, 2826–2843.

Bretherton, C. S., and M. C. Wyant (1997). Moisture transport, lower tropospheric stability and decoupling of cloud-topped boundary layers. *J. Atmos. Sci.* **54**, 148–167.

Businger, J. A., J. C. Wyngaard, Y. Izumi, and E. F. Bradley (1971). Flux-profile relationships in the atmospheric surface layer. *J. Atmos. Sci.* **28**, 181–189.

Chen, J.-M. (1991). Turbulence-scale condensation parameterization. *J. Atmos. Sci.* **48**, 1510–1512.

Deardorff, J. W. (1972). Parameterization of the planetary boundary layer for use in general circulation models. *Mon. Wea. Rev.* **100**, 93–106.

Deardorff, J. W. (1980). Cloud top entrainment instability. *J. Atmos. Sci.* **37**, 131–147.

Esbensen, S. K. and M. J. McPhaden (1996). Enhancement of tropical ocean evaporation and sensible heat flux by atmospheric mesoscale systems. *J. Climate* **9**, 2307–2325.

Fu, Q. (1991). Parameterization of radiative processes in vertically nonhomogeneous multiple scattering atmospheres. Ph.D. Dissertation, Dept. of Meteorology, University of Utah, Salt Lake City.

Fu, Q., S. K. Krueger, and K. N. Liou (1995). Interactions of radiation and convection in simulated tropical cloud clusters. *J. Atmos. Sci.* **52**, 1310–1328.

Glendening, J. W. (1994). Dependence of a plume heat budget upon lateral advection. *J. Atmos. Sci.* **51**, 3517–3530.

Glendening, J. W., and S. D. Burk (1992). Turbulent transport from an Arctic lead: A large-eddy simulation. *Bound.-Layer. Meteor.* **59**, 315–339.

Grabowski, W. W., X. Wu, and M. W. Moncrieff (1996). Cloud resolving modeling of tropical cloud systems during Phase III of GATE. Part I: Two-dimensional experiments. *J. Atmos. Sci.* **53**, 3684–3709.

Grabowski, W. W., X. Wu, M. W. Moncrieff, and W. D. Hall (1998). Cloud-resolving modeling of cloud systems during Phase III of GATE. Part II: Effects of resolution and the third spatial dimension. *J. Atmos. Sci.* **55**, 3264–3282.

Heymsfield, A. J., and L. J. Donner (1990). A scheme for parameterizing ice-cloud water content in general circulation models. *J. Atmos. Sci.* **47**, 1865–1877.

Heymsfield, A. J., L. M. Miloshevich, A. Slingo, K. Sassen, and D. O'C. Starr (1991). An observational and theoretical study of highly supercooled altocumulus. *J. Atmos. Sci.* **48**, 923–945.

Hignett, P. (1991). Observations of diurnal variation in a cloud-topped marine boundary layer. *J. Atmos. Sci.* **48**, 1474–1482.

Jabouille, P., J. L. Redelsperger, and J. P. Lafore (1996). Modification of surface fluxes by atmospheric convection in the TOGA-COARE region. *Mon. Wea. Rev.* **124**, 816–837.

Klein, S. A., D. L. Hartmann, and J. R. Norris (1994). On the relationships among low cloud structure, sea surface temperature, and atmospheric circulation in the summertime northeast Pacific. *J. Climate* **8**, 1140–1155.

Krueger, S. K. (1985). Numerical simulation of tropical cumulus clouds and their interaction with the subcloud layer. Ph.D. Dissertation, Dept. of Atmospheric Sciences, University of California, Los Angeles.

Krueger, S. K. (1988). Numerical simulation of tropical cumulus clouds and their interaction with the subcloud layer. *J. Atmos. Sci.* **45**, 2221–2250.

Krueger, S. K. (1993). Linear eddy modeling of entrainment and mixing in stratus clouds. *J. Atmos. Sci.* **50**, 3078–3090.

Krueger, S. K., and A. Bergeron (1994). Modeling the trade cumulus boundary layer. *Atmos. Res.* **33**, 169–192.

Krueger, S. K., Q. Fu, K. N. Liou, and H.-N. S. Chin (1995a). Improvements of an ice-phase microphysics parameterization for use in numerical simulations of tropical convection. *J. Appl. Meteor.* **34,** 281–287.

Krueger, S. K., G. T. McLean, and Q. Fu (1995b). Numerical simulation of the stratus-to-cumulus transition in the subtropical marine boundary layer. Part I: Boundary-layer structure. *J. Atmos. Sci.* **52,** 2839–2850.

Krueger, S. K., G. T. McLean, and Q. Fu (1995c). Numerical simulation of the stratus-to-cumulus transition in the subtropical marine boundary layer. Part II: Boundary-layer circulation. *J. Atmos. Sci.* **52,** 2851–2868.

Krueger, S. K., S. M. Lazarus, P. Bechtold, S. Chen, D. Cripe, L. Donner, W. Grabowski, M. Gray, D. Gregory, J. Gregory, F. Guichard, H. Jiang, D. Johnson, R. McAnelly, J. Petch, D. Randall, J.-L. Redelsperger, C. Seaman, H. Su, W.-K. Tao, X. Wu, and K.-M. Xu (2000). Intercomparison of multi-day simulations of convection during TOGA COARE using several cloud-resolving and single-column models. Submitted for publication.

Lazarus, S. M., S. K. Krueger, and G. G. Mace (2000). A cloud climatology of the Southern Great Plains ARM CART. Accepted for publication.

Lilly, D. K. (1968). Models of cloud-topped mixed layers under a strong inversion. *Quart. J. Roy. Meteor. Soc.* **94,** 292–309.

Liu, S. (1998). Numerical modeling of altocumulus cloud layers, Ph.D. Dissertation. Dept. of Meteorology, University of Utah, Salt Lake City.

Liu, S., and S. K. Krueger (1997). Effects of radiation in simulated altocumulus cloud layers. In "Preprints, Ninth Conference on Atmospheric Radiation," Long Beach, CA, pp. 330–334. Amer. Meteor. Soc.

Lord, S. J., H. E. Willoughby, and J. M. Piotrowicz (1984). Role of a parameterized ice-phase microphysics in an axisymmetric, nonhydrostatic tropical cyclone model. *J. Atmos. Sci.* **41,** 2836–2848.

Mahrt, L., and J. Sun (1995). The subgrid velocity scale in the bulk aerodynamic relationship for spatially averaged scalar fluxes. *Mon. Wea. Rev.* **123,** 3032–3041.

McCumber, M., W. K. Tao, J. Simpson, R. Penc, and S. T. Soong (1991). Comparison of ice-phase microphysical parameterization schemes using numerical simulations of convection. *J. Appl. Meteor.* **30,** 985–1004.

Moeng, C.-H. (1986). Large-eddy simulation of a stratus-topped boundary layer. Part I: Structure and budgets. *J. Atmos. Sci.* **43,** 2886–2900.

Moeng, C.-H., and A. Arakawa (1980). A numerical study of a marine subtropical stratus cloud layer and its stability. *J. Atmos. Sci.* **37,** 2661–2676.

Moeng, C.-H., S. Shen, and D. A. Randall (1992). Physical processes within the nocturnal stratus-topped boundary layer. *J. Atmos. Sci.* **49,** 2384–2401.

Moeng, C.-H., W. R. Cotton, C. Bretherton, A. Chlond, M. Khairoutdinov, S. K. Krueger, W. S. Lewellen, M. K. McVean, J. R. M. Pasquier, H. A. Rand, A. P. Siebesma, R. I. Sykes, B. Stevens (1996). Simulation of a stratocumulus-topped PBL: Intercomparison of different numerical codes. *Bull. Am. Meteor. Soc.* **77,** 216–278.

Randall, D. A. (1980). Conditional instability of the first kind upside-down. *J. Atmos. Sci.* **37,** 125–130.

Randall, D. A. (1984). Stratocumulus cloud-deepening through entrainment. *Tellus* **36A,** 446–457.

Redelsperger, J. L., P. R. A. Brown, F. Guichard, C. Hoff, M. Kawasima, S. Lang, T. Montmerle, K. Nakamura, K. Saito, C. Seman, W. K. Tao, and L. J. Donner (2000). A GCSS model intercomparison for a tropical squall line observed during TOGA-COARE. I: Cloud-resolving models. *Quart. J. Roy. Meteor. Soc.* **126,** 823–864.

Riehl, H., and J. S. Malkus (1958). On the heat balance of the equatorial trough zone. *Geophysica* **6,** 503–538.

Riehl, H., T. C. Yeh, J. S. Malkus, and N. E. La Seur (1951). The north-east trade of the Pacific Ocean. *Quart. J. Roy. Meteor. Soc.* **77,** 598–626.

Ryan, B. F. (1996). On the global variation of precipitating layer clouds. *Bull. Am. Meteor. Soc.,* **77,** 53–70.

Schubert, W. S., J. S. Wakefield, E. J. Steiner, and S. K. Cox (1979). Marine stratocumulus convection, Part II: Horizontally inhomogeneous solutions. *J. Atmos. Sci.* **36,** 1308–1324.

Siebesma, A. P., and J. W. M. Cuijpers (1995). Evaluation of parametric assumptions for shallow cumulus convection. *J. Atmos. Sci.* **52,** 650–666.

Sommeria, G. (1976). Three-dimensional simulation of turbulent processes in the undisturbed trade wind boundary layer. *J. Atmos. Sci.* **33,** 216–241.

Soong, S.-T., and K.-K. Tao (1980). Response of deep tropical cumulus clouds to mesoscale processes. *J. Atmos. Sci.* **37,** 2035–2050.

Soong, S.-T., and Y. Ogura (1980). Response of tradewind cumuli to large-scale processes. *J. Atmos. Sci.* **37,** 2016–2034.

Starr, D. O'C. and S. K. Cox (1985). Cirrus clouds. Part II: Numerical experiments on the formation and maintenance of cirrus. *J. Atmos. Sci.* **42,** 2682–2694.

Turton, J. D., and S. Nicholls (1987). A study of the diurnal variation of stratocumulus using a multiple mixed layer model. *Quart. J. R. Meteor. Soc.* **113,** 969–1009.

Wakefield, J. S., and W. S. Schubert (1981). Mixed-layer model simulation of Eastern North Pacific stratocumulus. *Mon. Wea. Rev.* **109,** 1952–1968.

Warren, S. G., C. J. Hahn, J. London, R. M. Chervin, and R. Jenne (1986). Global distribution of total cloud cover and cloud type amounts over land, NCAR Tech. Note TN-273 + STR.

Warren, S. G., C. J. Hahn, J. London, R. M. Chervin, and R. Jenne (1988). Global distribution of total cloud cover and cloud type amounts over ocean, NCAR Tech. Note TN-317 + STR.

Williams, A. G., H. Kraus, and J. M. Hacker (1996). Transport processes in the tropical warm pool boundary layer. Part I: Spectral composition of the fluxes. *J. Atmos. Sci.* **53,** 1187–1202.

Wu, X., W. W. Grabowski, and M. W. Moncrieff (1998). Long-term behavior of cloud systems in TOGA COARE and their interactions with radiative and surface processes. Part I: Two-dimensional modeling study. *J. Atmos. Sci.* **55,** 2693–2714.

Wyant, M. C., C. S. Bretherton, H. A. Rand, and D. E. Stevens (1997). Numerical simulations and a conceptual model of the stratocumulus to trade cumulus transition. *J. Atmos. Sci.* **54,** 168–192.

Xu, K.-M., and D. A. Randall (1996). Explicit simulation of cumulus ensembles with the GATE Phase III data: Comparison with observations. *J. Atmos. Sci.* **53,** 3710–3736.

Xu, K.-M., A. Arakawa, and S. K. Krueger (1992). The macroscopic behavior of cumulus ensembles simulated by a cumulus ensemble model. *J. Atmos. Sci.* **49,** 2402–2420.

Xu, K.-M., and S. K. Krueger (1991). Evaluation of cloudiness parameterizations using a cumulus ensemble model. *Mon. Wea. Rev.* **119,** 342–367.

Zulauf, M., and S. K. Krueger (1997). Parameterization of mesoscale enhancement of large-scale surface fluxes over tropical oceans. *In* "Preprints, 22nd Conference on Hurricanes and Tropical Meteorology," Fort Collins, CO, pp. 164–165. Amer. Meteor. Soc.

Zulauf, M. A., and S. K. Krueger (2000). Parameterization of mesoscale enhancement of large-scale surface fluxes over Tropical oceans. Submitted for publication.

Zulauf, M. A., and S. K. Krueger (1999). Two-dimensional numerical simulations of Arctic leads. *In* "Preprints, Fifth Conference on Polar Meteorology and Oceanography," Dallas, TX, pp. 404–408. Amer. Meteor. Soc.